

# Dynamical phase transition in an open quantum system

Ling-Na Wu<sup>1,3</sup>, Jens Nettersheim<sup>2,3</sup>, Julian Feß<sup>2</sup>, Alexander Schnell<sup>1</sup>, Sabrina Burgardt<sup>2</sup>, Silvia Hiebel<sup>2</sup>, Daniel Adam<sup>2</sup>, André Eckardt<sup>1,4</sup>, and Artur Widera<sup>2,5</sup>

<sup>1</sup>Institut für Theoretische Physik, Technische Universität Berlin, Hardenbergstraße 36, 10623 Berlin, Germany <sup>2</sup>Department of Physics and State Research Center OPTIMAS, Technische Universität Kaiserslautern, 67663 Kaiserslautern, Germany <sup>3</sup>These authors contributed equally to this work: Ling-Na Wu and Jens Nettersheim. <sup>4</sup>email: eckardt@tu-berlin.de <sup>5</sup>email: widera@physik.uni-kl.de

August 11, 2022

**Phase transitions correspond to the singular behavior of physical systems in response to continuous control parameters like temperature or external fields [1]. Near continuous phase transitions, associated with the divergence of a correlation length, universal power-law scaling behavior with critical exponents independent of microscopic system details is found. Recently, dynamical quantum phase transitions and universal scaling have been predicted and also observed in the non-equilibrium dynamics of isolated quantum systems after a quench, with time playing the role of the control parameter [2–10]. However, signatures of such dynamical phase transition in open systems, whose dynamics is driven by the dissipative contact to an environment, were so far elusive. Here, we demonstrate that dynamical phase transitions with respect to time can also occur in open quantum systems described by mixed states. We experimentally measure the relaxation dynamics of the large atomic spin of individual Caesium atoms induced by the dissipative coupling via spin-exchange processes to an ultracold Bose gas of Rubidium atoms. For initial states far from equilibrium, the entropy of the spin state is found to peak in time, transiently approaching its maximum possible value, before eventually relaxing to its lower equilibrium value. This effect is associated with a prethermal loss of the system’s memory of the details of the initial state [11]. Moreover, a finite-size scaling analysis based on numerical simulations shows that it corresponds to a dynamical phase transition of the dissipative system in the limit of large system sizes. Our results show that dynamical phase transitions are not restricted to occur in isolated systems, but, surprisingly, are possible also during the dissipative evolution of open quantum systems.**

Phase transitions emerge from the collective behavior of large quantum systems in the thermodynamic limit [1]. A continuous phase transition is signaled by the diver-

gence of a characteristic length scale  $\xi$ , when the control parameter approaches a critical value. As a result, the behavior near the transition becomes independent of the microscopic details of a system, giving rise to universal critical exponents [1], like the one describing the divergence of  $\xi$  as a function of the control parameter. Despite the fact that the distinction between different phases of matter, like liquid or crystalline, is an essential and well-known aspect of nature, phase transitions remain an active field of research until today. Subjects of interest include, for instance, quantum phase transitions happening in pure quantum ground states at absolute zero [12] and topological phase transitions beyond Landau’s paradigm [13].

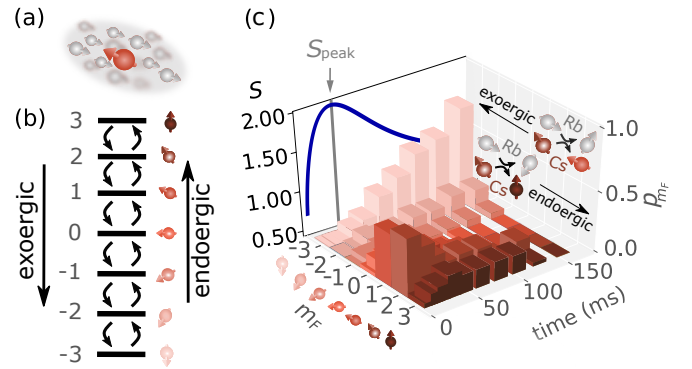


**Figure 1 | Realizing an open spin system** (a) Individual Cs atom (red) interacting with a bath of spin-polarized Rb atoms via inelastic spin-exchange (SE) collisions. (b) The Cs-Zeeman states experimentally realize an equidistant seven-level ( $m_F \in \{3, 2, \dots, -3\}$ ) spin system defining  $m_F = -3$  as ground state for the Rb-Cs compound (for more details, see Methods). SE collisions with the Rb atoms give rise to dissipative spin dynamics, increasing (decreasing) internal energy and angular momentum for endoergic (exoergic) processes. The twelve SE rates between the Cs Zeeman states depend on the external magnetic field and the bath temperature. (c) Bath-driven and time-resolved quantum-spin evolution for individual Cs atoms initially prepared in a mixture of  $|m_F = 1\rangle$  and  $|m_F = 2\rangle$ . Sketches in the back panel show the microscopic collision processes of exoergic and endoergic SE collisions. The lateral plane shows the resulting entropy evolution, featuring a maximum at  $S_{\text{peak}} = 1.944 \approx \ln 7 = S_{\text{max}}$ .

Recently, the transient evolution of isolated quantum systems gained considerable interest, as it can be realized in engineered quantum systems such as ultracold atomic quantum gases. Prominent effects that were studied include the transition between eigenstate thermalization and

many-body localization [14–16], non-equilibrium phase transitions in the long-time (or prethermal) behavior of (almost) integrable quantum systems [17, 18], or the observation of discrete-time crystals in interacting Floquet systems [19, 20]. Another fascinating example is the prediction and observation of dynamical quantum phase transitions [7–10] and universal scaling behavior [2–6] occurring at a critical time during the transient non-equilibrium evolution of isolated quantum systems. Here *time* plays the role of the control parameter. The underlying non-equilibrium dynamics can be initialized, for example, by a quantum quench, i.e., a rapid parameter variation starting from the ground state of the previous Hamiltonian.

In the following, we demonstrate that dynamical phase transitions, where time plays the role of the control parameter, can equally occur in the transient evolution of *open* systems. Importantly, such dynamical phase transitions, occurring at a critical time, are markedly different from non-equilibrium phase transitions emerging in the non-equilibrium steady states of driven-dissipative systems (while a simple example is given by the lasing transition, more complex scenarios can occur, see, e.g., Ref. [22] and references therein).

In contrast to isolated quantum systems, open quantum systems [23] are characterized by the coupling to an environment, called a bath, with which they exchange both energy and information. Markovian baths rapidly dissipate information, so that the dynamics of the system can be described by an idealized time-local master equation  $\dot{\rho}(t) = \mathcal{L}[\rho(t)]$ , where the dynamics are generated by a time-independent Liouvillian superoperator  $\mathcal{L}$  acting on the instantaneous density operator  $\rho(t)$  describing the system's state at time  $t$ . If the coupling to the environment is weak compared to the level spacing in the system,  $\rho(t)$  quickly becomes diagonal with respect to the energy eigenstates  $|m\rangle$ ,  $\rho(t) \simeq \sum_m p_m(t) |m\rangle\langle m|$ . The probabilities  $p_m(t)$  for being in state  $|m\rangle$  then follow a Pauli rate equation  $\dot{p}_m = \sum_{m' \neq m} [R_{mm'} p_{m'} - R_{m'm} p_m]$ , with  $R_{mm'}$  denoting the rate for a bath-induced transition from  $|m'\rangle$  to  $|m\rangle$  [23].

In systems of ultracold atoms, dissipation can be engineered in various ways, including, for instance, the coupling of the atoms to a cavity [24], spontaneous emission of lattice photons [25, 26], particle loss (e.g. via controlled ionization [27]), or the coupling to a background gas [28]. We realize such an open system by the spin degrees of freedom of individual ultracold Caesium atoms ( $^{133}\text{Cs}$ ), which are immersed as impurities in a bath comprising ultracold Rubidium atoms ( $^{87}\text{Rb}$ ) [see the sketch in Fig. 1(a) and Methods for details]. The hyperfine states of both species form stable quasi-spins with quantum num-

bers  $F = 3$  ( $F = 1$ ) for Cs (Rb). In the presence of a weak, constant external magnetic field  $B$ , the spins possess an equidistant ladder spectrum  $E_{m_F} = m_F \Delta$ , where  $\Delta = g_F \mu_B B / \hbar$ , with Landé factor  $g_F$ , reduced Planck constant  $\hbar$  and Bohr magneton  $\mu_B$ . The corresponding energy eigenstates  $|m_F\rangle$  are characterized by the magnetic quantum number  $m_F = -F, -F + 1, \dots, F$ . Elastic Rb-Cs collisions quickly thermalize the Cs atoms' center-of-mass motion, while inelastic spin-exchange (SE) processes give rise to bath-induced transitions, where the Cs spins are changed by single quanta of angular momentum,  $m_F \rightarrow m'_F = m_F \pm 1$  with corresponding rates  $R_{\pm, m_F} \equiv R_{m_F \pm 1, m_F}$  [29], see Fig. 1(b) and Methods ( $m_F$  is used throughout for the Cs spins). We initially prepare the Cs impurity in an excited spin state defined by the probability distribution  $p_{m_F}(0)$ , and monitor the subsequent relaxation dynamics  $p_{m_F}(t)$ ; see Fig. 1(c) for an example. As an important observable, we extract the evolution of the dimensionless (setting Boltzmann's constant  $k_B = 1$ ) spin entropy [blue curve in Fig. 1(c)],

$$S(t) = - \sum_{m_F} p_{m_F}(t) \ln(p_{m_F}(t)). \quad (1)$$

In Fig. 2(a) and (b), we show the measured evolution of  $S$  for various different initial conditions (specified in the insets). This paper's blue and red background colors indicate unidirectional and bidirectional spin-exchange. For highly excited initial states, that means for the Rb-Cs compound states of large positive  $m_F$  (for more details, see Methods), we find in both scenarios that the entropy evolution is highly non-monotonous. The entropy first increases to reach a peak value  $S_{\text{peak}}$  at a time  $t_{\text{peak}}$ , before eventually relaxing to a steady-state. This is remarkable and rather different from the behavior found for initial states close to equilibrium, for which we observe that the entropy simply increases in time until it saturates at its steady-state value [see pink curve in Fig. 2(b)]. Even more remarkably, for various different initial conditions, this peak value almost reaches the maximal possible entropy,  $S_{\text{max}} = \ln M$  with  $M = 7$  being the number of spin states, indicated by the dashed line.

The approach of  $S_{\text{max}}$  implies that the system transiently approaches the maximally mixed state  $\rho_{\text{max}} = M^{-1} \sum_{m_F} |m_F\rangle\langle m_F|$ , corresponding to a completely delocalized spin distribution  $p_{m_F} = 1/M$ . In the limit of large  $M$ , such behavior implies a divergence of both  $S$  and the length  $\xi$  associated with the broadness of the distribution  $p_{m_F}$  in state-space.<sup>1</sup> This, in turn, directly corresponds to the divergence of a relevant length scale  $\xi$  that

<sup>1</sup>There are different possibilities to define  $\xi$ . Two examples are given by the participation ratio  $\xi \equiv (\sum_{m_F} p_{m_F}^2)^{-1}$  and  $\xi \equiv \exp(S)$ .

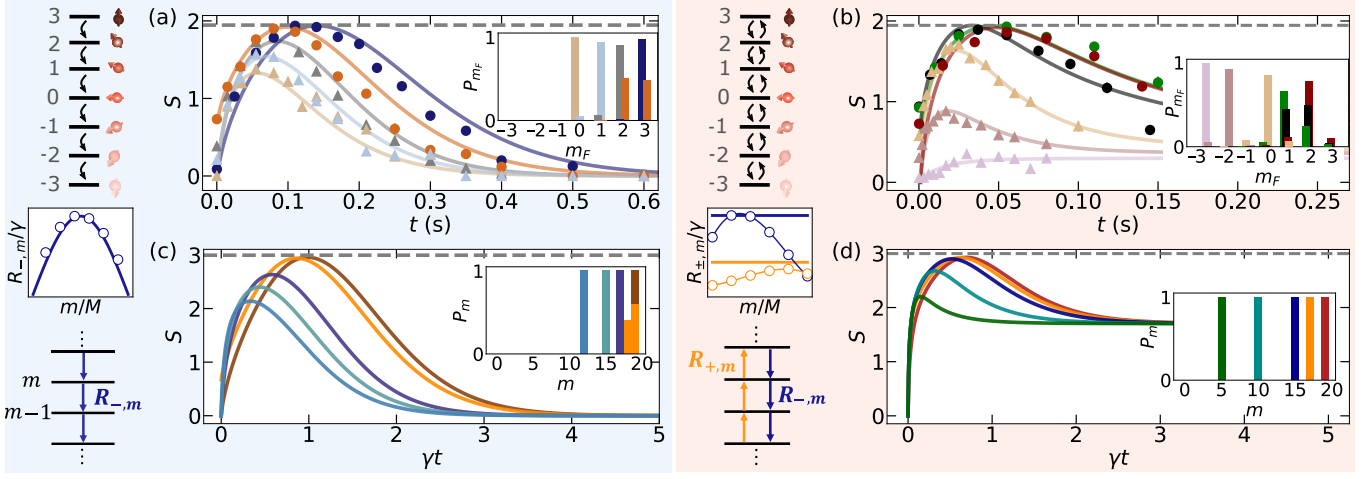


**Figure 2 | Entropy evolution** Blue (red) background indicates regimes where unidirectional spin transitions, applying a high magnetic field ( $B = 460$  mG) and bidirectional spin transitions, utilizing a low magnetic field ( $B = 25$  mG) are possible. While in the former case, endoergic transitions are suppressed completely [21], in the latter case, they are allowed and raise  $m_F$  for Cs, but with reduced probability compared to exoergic processes, which lower  $m_F$ . (a, b) Experimentally measured entropy evolution starting from different initial states shown in the insets (colors match). Bullets ( $\bullet$ ) are used for trajectories with high peak entropy ( $S_{\text{peak}} \geq 0.98S_{\text{max}}$ ) and triangles ( $\blacktriangle$ ) otherwise. Error bars are smaller than symbol sizes and represent the standard deviation. Solid lines are obtained from simulations, dashed lines indicate maximum possible entropy  $S_{\text{max}}$ . (c, d) Like (a, b) but for theoretical models with 20 states. Panels between the level schemes show normalized transfer rates for the experimental system (dots) and the theoretical models (lines). For the unidirectional model (in blue background),  $R_{-,m} = \gamma M \sin(\pi(m+1)/M)$ , where  $\gamma$  is the coupling strength. For the bidirectional model (red background), thick horizontal lines correspond to the state-independent-rate model discussed in the main text, with  $R_{+,m} \equiv R_+ = \gamma M$  (orange) and  $R_{-,m} \equiv R_- = \gamma M \exp(10/M)$  (blue). Thin curves correspond to the state-dependent-rate model discussed in the supplemental material.

is found when a system approaches a continuous phase transition. Here, however, the continuous control parameter is the time  $t$  and its critical value is  $t_{\text{peak}}$ . In this sense, a transient approach of the maximally mixed state  $\rho_{\text{max}}$ , indicates a dynamical phase transition in the limit of large  $M$ .

To answer the question whether the observed dynamics is indeed a finite-size precursor of such a dynamical phase transition, we define two model systems of variable system size  $M$  [see Fig. 2 middle and lower side panels] and numerically perform a finite-size scaling analysis to extract the behavior for  $M \rightarrow \infty$ . Both models consist of  $M$  states labeled by  $m = 0, 1, \dots, M-1$ , which form an equidistant energy spectrum  $\varepsilon_m = m\Delta$ . A unidirectional model generalizes the high-magnetic-field regime to larger  $M$ . Here, only transitions  $|m\rangle \rightarrow |m' = m-1\rangle$  occur, corresponding to a zero-temperature bath. The rates  $R_{-,m}$  possess a parabolic dependence on  $m$  mimicking the experimental rates, which is crucial for reaching high peak entropies. In a bidirectional model, corresponding to the case of low magnetic fields, it is sufficient to assume state independent rates<sup>2</sup>  $R_{\pm,m} \equiv R_{\pm}$ . Such rates

correspond to a bath of finite inverse temperature  $\beta$ , with  $R_+/R_- = \exp(-\beta\Delta)$ . Figs. 2(c) and (d) depict the entropy evolution for both models with  $M = 20$  for various initial conditions. Again  $S_{\text{peak}} \approx S_{\text{max}}$  is found for highly excited initial states.

To compare data for different initial conditions, we introduce the effective inverse temperature

$$\beta_{\text{eff}} \equiv \frac{dS/dt}{dE/dt} = \frac{dS}{dE}, \quad (2)$$

with mean energy  $E$ , as a scaled control parameter. It is monotonically related to the time  $t$  (see supplemental material for more details) and becomes zero at  $t = t_{\text{peak}}$ , while it takes negative (positive) values for  $t < t_{\text{peak}}$  ( $t > t_{\text{peak}}$ ). In Figs. 3(a) and (d), the measured entropy is plotted as a function of  $\beta_{\text{eff}}$ . For those initial conditions giving rise to close-to-maximum peak entropies, marked by bullets, the data collapse in the vicinity of  $\beta_{\text{eff}} = 0$ .

Assuming a continuous phase transition in the thermodynamic limit,  $M \rightarrow \infty$ , the length  $\xi$  is expected to diverge like  $\xi \propto \beta_{\text{eff}}^{-\nu}$  at the critical inverse temperature  $\beta_{\text{eff}}^{(c)} = 0$ , where  $\nu$  is a critical exponent. As a consequence, in the vicinity of the transition, the system's behavior should depend on the ratio of  $\xi$  and the system size

Both give rise to the same maximum value  $\xi_{\text{max}} = M$ , which is uniquely assumed for the maximally mixed state  $\rho_{\text{max}}$ .

<sup>2</sup>Results for  $m$ -dependent rates, mimicking the experimental ones,

are similar and presented in the supplemental material.

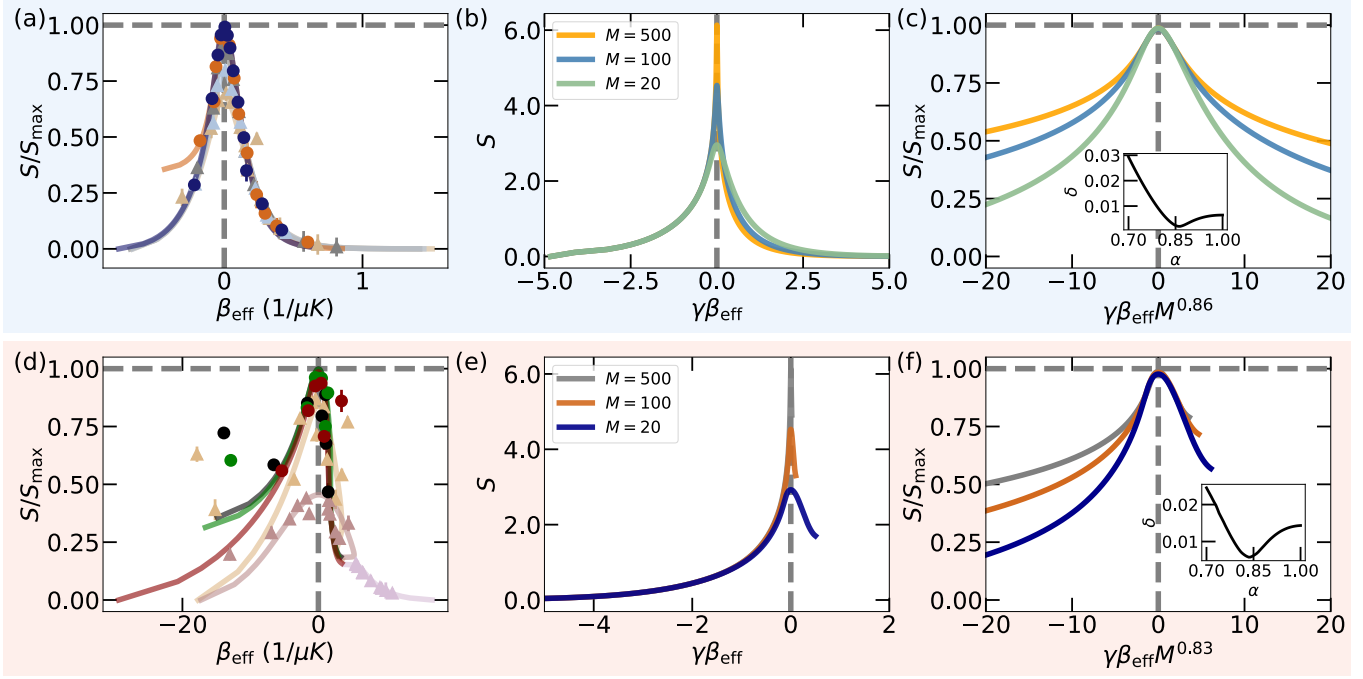


**Figure 3 | Finite-size scaling.** (a, d) Experimentally measured (symbols) and simulated (lines) entropy plotted as a function of  $\beta_{\text{eff}}$  [data, colors, and symbols like in Fig. 2(a,b)]. (b, e) The entropy of simulated model systems starting from the most excited state vs.  $\beta_{\text{eff}}$  for different system sizes  $M$ . (c, f) The curves from (b,e) collapse around  $\beta_{\text{eff}} = 0$  when the entropy normalized with  $S_{\text{max}}$  is plotted vs. the scaled parameter  $\beta_{\text{eff}} M^\alpha$ , where the exponent  $\alpha$  is fixed by comparing the mean difference  $\delta$  between the data with  $\gamma\beta_{\text{eff}} M^\alpha \in [-2, 2]$ , as shown in the inset (see supplemental material for more detail). Note that the transfer rates in the bidirectional model (with red background) are defined to scale linearly with system size  $M$ , which leads to the disappearance of peak entropy in the thermodynamic limit since the steady-state entropy reaches the maximal possible value  $S_{\text{max}}$ . Vertical dashed lines mark  $\beta_{\text{eff}} = 0$ . Background colors as in Fig. 2.

$M$ , only, or, equivalently on  $(\xi/M)^{-1/\nu} = \beta_{\text{eff}} M^{1/\nu}$ . In particular, we expect the entropy  $S$  to show the universal scaling behavior  $S \simeq S_{\text{max}} g(\beta_{\text{eff}} M^{1/\nu})$  in the vicinity of the transition, with some function  $g$ . In Figs. 3(b) and (e), we plot  $S$  as a function of  $\beta_{\text{eff}}$  for different system sizes  $M$  for both models. The data are obtained from the simulated time evolution starting from the most excited state. Plotting the scaled entropy  $S/S_{\text{max}}$  as a function of scaled  $\beta_{\text{eff}}$  in Figs. 3(c) and (f), we find indeed that the curves collapse near  $\beta_{\text{eff}} = 0$  for both of the model systems. This shows that the observed transient approach of the maximally mixed state  $\rho_{\text{max}}$  is (a finite-size precursor of) a dynamical phase transition. Remarkably, the corresponding critical exponent for the associated diverging length scale  $\xi$  appears to be independent of the system's details, suggesting universal scaling behavior. Namely, it takes the value  $\nu \approx 1/0.85$  for the two model systems discussed in the main text and for the bidirectional model with state-dependent rates, which is discussed in the supplemental material. In the supplemental material we, moreover, provide additional analyses, including: (i) a discussion of the phase transition with time playing the role of the control parameter, rather than  $\beta_{\text{eff}}$ ; (ii) the estimation of critical

exponent for the effective specific heat  $C = dE/d(\beta_{\text{eff}}^{-1})$ , which equally shows universal behavior; as well as (iii) a finite-size scaling analysis entirely based on experimental results, which, however, is limited to the rather small system sizes  $M = 3, 5, 7$ .

Since the maximum entropy  $S_{\text{max}}$  corresponds to a unique state, the maximally mixed state  $\rho_{\text{max}}$ , after approaching  $S_{\text{max}}$ , the dynamics is expected to become independent of the details of the initial state. This happens long before the spin system has thermalized [11]. Such a prethermal memory loss is observed in the experiment for both magnetic field regimes. In Figs. 4(a)-(c), we show the entropy evolution and the population dynamics of two spin states versus the shifted time  $t - t_{\text{peak}}$  in the regime of unidirectional rates (corresponding plots for the bidirectional regime are presented in the supplemental material). We can see that the data with a high peak entropy ( $S_{\text{peak}} \geq 0.98 S_{\text{max}}$ , indicated by bullets) show similar behavior for both the entropy evolution and spin dynamics after the system reaches peak entropy ( $\tau \equiv t - t_{\text{peak}} > 0$ ).

To quantify this observation, we introduce the distance

$$\chi_{ij}(\tau) = \frac{1}{M} \sum_{m=1}^M |p_m^{(i)}(t_{\text{peak}}^{(i)} + \tau) - p_m^{(j)}(t_{\text{peak}}^{(j)} + \tau)| \quad (3)$$

between two trajectories with different initial conditions,  $p_{m_F}^{(i)}(0)$  and  $p_{m_F}^{(j)}(0)$ , and peak times  $t_{\text{peak}}^{(i)}$  and  $t_{\text{peak}}^{(j)}$  or, equivalently, the respective  $\beta_{\text{eff}}$ . For the experimental data we compare each trajectory  $p_{m_F}^{(i)}$  to the optimal trajectory  $p_{m_F}^{\text{max}}(t)$  defined by  $S_{\text{peak}} = S_{\text{max}}$ . In Fig. 4(d), we plot the corresponding distance  $\chi_i \equiv \chi_{i\text{max}}$  versus  $\beta_{\text{eff}}$ . For those trajectories featuring large peak entropies,  $\chi_i$  becomes small at the transition  $\beta_{\text{eff}} = 0$ . In comparison, for trajectories with  $S_{\text{peak}} < 0.98S_{\text{max}}$  (indicated by triangles)  $\chi_i$  remains large after the transition.

Prethermal memory loss is also found in the theoretical models. Here we have easy access to many initial conditions and, therefore, we can compute the mean distance  $\chi \equiv \text{mean}_{ij \in \mathcal{U}}(\chi_{ij})$  of those trajectories whose peak entropies  $S_{\text{peak}}$  are close to the maximal entropy, i.e., for which  $S_{\text{peak}}/S_{\text{max}} > 1 - \delta S$  with threshold  $\delta S \ll 1$ . Fig. 4(e) plots normalized  $\chi$  versus  $\beta_{\text{eff}}$  for different system sizes with  $\delta S = 0.2$ . One can see that for increasing  $M$  a sharp transition forms at  $\beta_{\text{eff}} = 0$ .

In summary, we have investigated the far-from-equilibrium relaxation dynamics of an open quantum system given by a large spin coupled to a bath. We find that for highly excited initial states, the system transiently approaches the maximally mixed state  $\rho_{\text{max}}$ , as signaled by a peak in the entropy evolution approximately reaching the maximally possible value  $S_{\text{max}}$ . We show that, when reaching the entropy peak, the dynamics shows distinct features that signal a continuous phase transition with time playing the role of the control parameter: (i) In the limit of large system sizes, the localization length  $\xi$  characterizing the spin state, diverges at the transition. (ii) A finite-size scaling analysis reveals a power-law scaling  $\xi \sim \beta_{\text{eff}}^{-\nu}$  near the transition, with respect to the scaled control parameter  $\beta_{\text{eff}}$ , which is monotonically related to time and allows to compare data for different initial states by locating the transition to  $\beta_{\text{eff}} = 0$ . (iii) The extracted critical exponent takes the same value  $\nu \approx 1/0.85 \approx 1.2$  for all model parameters considered, suggesting universal scaling behavior independent of the microscopic details of the system. Thus, we have demonstrated that a dynamical phase transition can not only occur in the evolution of isolated systems described by pure states but also during the dynamics of an open system induced by dissipation. It will be interesting to further investigate the nature of dynamical phase transitions in open quantum systems, including their non-equilibrium universality classes (to the exploration of

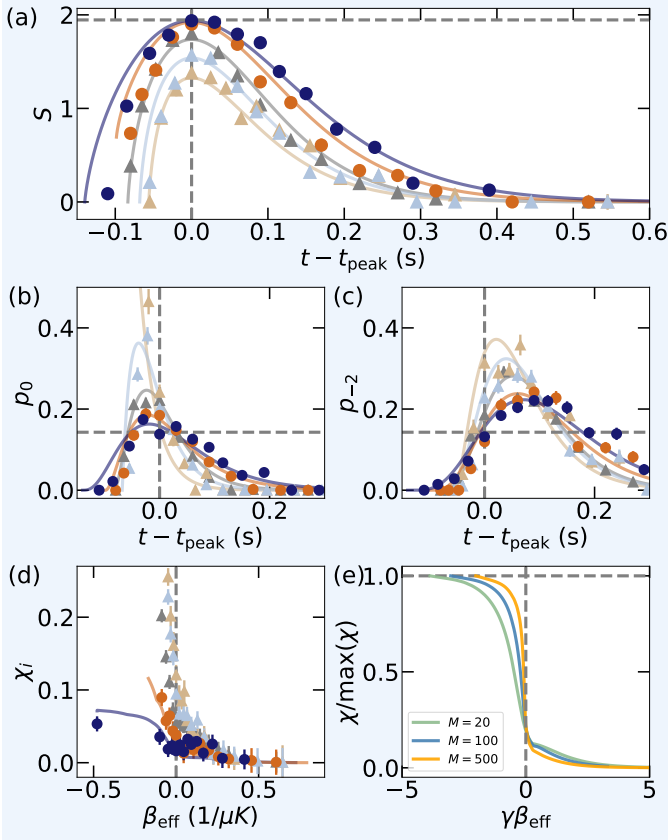


**Figure 4 | Prethermal memory loss.** (a) Experimentally measured (symbols) and simulated (lines) entropy for different initial conditions (color coding as in Fig. 2(a)) and (b, c) the corresponding population  $p_{m_F}$  for the two spin states (b)  $|m_F = 0\rangle$  and (c)  $|m_F = -2\rangle$  as a function of shifted time (by the peak entropy time  $t_{\text{peak}}$ ) for the unidirectional model. The dependency of  $\chi$  (see text for the definition) on the effective inverse temperature  $\beta_{\text{eff}}$  is shown in (d) for the experiments and in (e) for the theoretical model. Horizontal grey dashed lines mark the maximal entropy  $S_{\text{max}}$  in (a), the population  $1/7$  in (b, c) that corresponds to  $S_{\text{max}}$ , and  $1$  in (e). Vertical dashed lines mark  $t = t_{\text{peak}}$  and  $\beta_{\text{eff}} = 0$ , respectively.



which our results provide a first step and a new approach). Another subject for future theoretical and experimental exploration is the collective behaviour of many atoms in contact with the bath as it results both from quantum statistics as well as from potential interactions. Also the regime of stronger system-bath coupling, where non-markovian effects are expected, offers an intriguing perspective.

We thank Markus Heyl, Eric Lutz, and Li You, for their useful comments on the manuscript. This work was supported by the Deutsche Forschungsgemeinschaft (DFG, German Research Foundation) via the Collaborative Research Centers SFB/TR185 (Project No. 277625399) and SFB 910 (Project No. 163436311). S.B. acknowledges funding from Studienstiftung des deutschen Volkes.

1. Domb, C. *Phase transitions and critical phenomena* (Elsevier, 2000).
2. Berges, J., Rothkopf, A. & Schmidt, J. Non-thermal fixed points: Effective weak coupling for strongly correlated systems far from equilibrium. *Phys. Rev. Lett.* **101**, 041603 (2008). URL <https://link.aps.org/doi/10.1103/PhysRevLett.101.041603>.
3. Prüfer, M. *et al.* Observation of universal dynamics in a spinor bose gas far from equilibrium. *Nature* **563**, 217–220 (2018). URL <https://doi.org/10.1038/s41586-018-0659-0>.
4. Erne, S., Bücken, R., Gasenzer, T., Berges, J. & Schmiedmayer, J. Universal dynamics in an isolated one-dimensional bose gas far from equilibrium. *Nature* **563**, 225–229 (2018). URL <https://doi.org/10.1038/s41586-018-0667-0>.
5. Eigen, C. *et al.* Universal prethermal dynamics of bose gases quenched to unitarity. *Nature* **563**, 221–224 (2018). URL <https://doi.org/10.1038/s41586-018-0674-1>.
6. Schmied, C.-M., Mikheev, A. N. & Gasenzer, T. Non-thermal fixed points: Universal dynamics far from equilibrium. *Int. J. Mod. Phys. A* **34**, 1941006 (2019).
7. Heyl, M., Polkovnikov, A. & Kehrein, S. Dynamical quantum phase transitions in the transverse-field ising model. *Phys. Rev. Lett.* **110**, 135704 (2013). URL <https://link.aps.org/doi/10.1103/PhysRevLett.110.135704>.
8. Jurcevic, P. *et al.* Direct observation of dynamical quantum phase transitions in an interacting many-body system. *Phys. Rev. Lett.* **119**, 080501 (2017). URL <https://link.aps.org/doi/10.1103/PhysRevLett.119.080501>.
9. Fläschner, N. *et al.* Observation of dynamical vortices after quenches in a system with topology. *Nat. Phys.* **14**, 265 (2018).
10. Heyl, M. Dynamical quantum phase transitions: a review. *Reports on Progress in Physics* **81**, 054001 (2018). URL <https://doi.org/10.1088/1361-6633/aaaf9a>.
11. Wu, L.-N. & Eckardt, A. Prethermal memory loss in interacting quantum systems coupled to thermal baths. *Phys. Rev. B* **101**, 220302 (2020). URL <https://link.aps.org/doi/10.1103/PhysRevB.101.220302>.
12. Sachdev, S. *Quantum Phase Transitions* (Cambridge University Press, 2011), 2 edn.
13. Wen, X.-G. Colloquium: Zoo of quantum-topological phases of matter. *Rev. Mod. Phys.* **89**, 041004 (2017). URL <https://link.aps.org/doi/10.1103/RevModPhys.89.041004>.
14. Nandkishore, R. & Huse, D. A. Many-body localization and thermalization in quantum statistical mechanics. *Annual Review of Condensed Matter Physics* **6**, 15–38 (2015). URL <https://doi.org/10.1146/annurev-conmatphys-031214-014726>.
15. Polkovnikov, A., Sengupta, K., Silva, A. & Vengalattore, M. Colloquium: Nonequilibrium dynamics of closed interacting quantum systems. *Rev. Mod. Phys.* **83**, 863–883 (2011). URL <https://link.aps.org/doi/10.1103/RevModPhys.83.863>.
16. Choi, J.-y. *et al.* Exploring the many-body localization transition in two dimensions. *Science* **352**, 1547–1552 (2016).
17. Albiez, M. *et al.* Direct observation of tunneling and nonlinear self-trapping in a single bosonic josephson junction. *Phys. Rev. Lett.* **95**, 010402 (2005). URL <https://link.aps.org/doi/10.1103/PhysRevLett.95.010402>.

18. Marino, J., Eckstein, M., Foster, M. S. & Rey, A. M. Dynamical phase transitions in the collisionless pre-thermal states of isolated quantum systems: theory and experiments. *arXiv e-prints* arXiv:2201.09894 (2022). 2201.09894.
19. Khemani, V., Lazarides, A., Moessner, R. & Sondhi, S. L. Phase structure of driven quantum systems. *Phys. Rev. Lett.* **116**, 250401 (2016). URL <https://link.aps.org/doi/10.1103/PhysRevLett.116.250401>.
20. Else, D. V., Bauer, B. & Nayak, C. Floquet time crystals. *Phys. Rev. Lett.* **117**, 090402 (2016). URL <https://link.aps.org/doi/10.1103/PhysRevLett.117.090402>.
21. Bouton, Q. *et al.* Single-atom quantum probes for ultracold gases boosted by nonequilibrium spin dynamics. *Phys. Rev. X* **10**, 011018 (2020). URL <https://link.aps.org/doi/10.1103/PhysRevX.10.011018>.
22. Sieberer, L. M., Buchhold, M. & Diehl, S. Keldysh field theory for driven open quantum systems. *Reports on Progress in Physics* **79**, 096001 (2016).
23. Breuer, H.-P., Petruccione, F. *et al.* *The theory of open quantum systems* (Oxford University Press on Demand, 2002).
24. Ritsch, H., Domokos, P., Brennecke, F. & Esslinger, T. Cold atoms in cavity-generated dynamical optical potentials. *Rev. Mod. Phys.* **85**, 553–601 (2013). URL <https://link.aps.org/doi/10.1103/RevModPhys.85.553>.
25. Pichler, H., Schachenmayer, J., Daley, A. J. & Zoller, P. Heating dynamics of bosonic atoms in a noisy optical lattice. *Phys. Rev. A* **87**, 033606 (2013). URL <https://link.aps.org/doi/10.1103/PhysRevA.87.033606>.
26. Lüschen, H. P. *et al.* Signatures of many-body localization in a controlled open quantum system. *Phys. Rev. X* **7**, 011034 (2017). URL <https://link.aps.org/doi/10.1103/PhysRevX.7.011034>.
27. Brazhnyi, V. A., Konotop, V. V., Pérez-García, V. M. & Ott, H. Dissipation-induced coherent structures in bose-einstein condensates. *Phys. Rev. Lett.* **102**, 144101 (2009). URL <https://link.aps.org/doi/10.1103/PhysRevLett.102.144101>.
28. Diehl, S. *et al.* Quantum states and phases in driven open quantum systems with cold atoms. *Phys. Rev. Lett.* **102**, 144101 (2009). URL <https://link.aps.org/doi/10.1103/PhysRevLett.102.144101>.
29. Schmidt, F. *et al.* Tailored single-atom collisions at ultralow energies. *Phys. Rev. Lett.* **122**, 013401 (2019). URL <https://link.aps.org/doi/10.1103/PhysRevLett.122.013401>.
30. Kerman, A. J., Vuletić, V., Chin, C. & Chu, S. Beyond optical molasses: 3d raman side-band cooling of atomic cesium to high phase-space density. *Phys. Rev. Lett.* **84**, 439–442 (2000). URL <https://link.aps.org/doi/10.1103/PhysRevLett.84.439>.
31. Schmidt, F. *et al.* Precision measurement of the  $^{87}\text{Rb}$  tune-out wavelength in the hyperfine ground state  $f = 1$  at 790 nm. *Phys. Rev. A* **93**, 022507 (2016). URL <https://link.aps.org/doi/10.1103/PhysRevA.93.022507>.
32. Schmidt, F. *et al.* Quantum spin dynamics of individual neutral impurities coupled to a bose-einstein condensate. *Phys. Rev. Lett.* **121**, 130403 (2018). URL <https://link.aps.org/doi/10.1103/PhysRevLett.121.130403>.

## Methods

### Initial state preparation

Experimentally, the Rb bath is prepared by laser-cooling in a magneto-optical trap (MOT) and subsequent cooling by evaporation while the sample is trapped in a crossed dipole trap at a wavelength of  $\lambda = 1064$  nm. The bath's internal state is prepared via an optical pumping in  $|F_{\text{Rb}} = 1, m_{F,\text{Rb}} = 1\rangle$  and then transferred via the radio-frequency transition  $|F_{\text{Rb}} = 1, m_{F,\text{Rb}} = 1\rangle \rightarrow |F_{\text{Rb}} = 1, m_{F,\text{Rb}} = 0\rangle$  to a magnetic-field insensitive state. This allows us to accumulate Cs atoms from the atomic background vapor by laser cooling in a MOT only approximately  $200 \mu\text{m}$  apart from the Rb sample. Subsequently, a crossed dipole trap with a wavelength of  $\lambda$  loads the atoms from the MOT. Degenerate Raman sideband cooling [30] reduces the Cs temperature further while at the same time populating the bare atoms' absolute ground state  $|F_{\text{Cs}} = 3, m_{F,\text{Cs}} = 3\rangle$ . Microwave-driven Landau-Zener transitions near-resonant to the  $|F_{\text{Cs}} = 3\rangle \rightarrow |F_{\text{Cs}} = 4\rangle$  hyperfine transition ( $h \times 9.1$  GHz) prepare the Cs atoms in the desired initial state.

The interaction between Cs and Rb is initialized by transporting the Cs atoms into the bath via a species-selective optical lattice [31]. The interaction stops after applying a resonant laser pulse that pushes the Rb atoms out of the trap. Eventually, state-selective fluorescence imaging [32] yields the internal state and position of the Cs atoms.

### Experimental parameters

The bath temperature  $T$  and density  $n$  for each measurement are inferred from time-of-flight measurements of the Rb cloud on the one hand; and from comparing the seven measured  $m_F$ -state trajectories with hundreds of simulated state trajectories on the other hand. Each simulation contains slightly different bath parameters. The bath parameters yielding the smallest least-squares ( $\chi^2$ ) error for all trajectories and the independent time-of-flight measurement was used for the respective measurement data set. The individual parameters of each measurement and the corresponding initial population are listed in the supplemental material. For simplicity, Table 1 shows the mean temperature and mean density of all best-fitting parameters for the unidirectional, respectively, bidirectional experimental system. Moreover, the magnetic field is calibrated via microwave spectroscopy on the  $|F_{\text{Rb}} = 1, m_{F,\text{Rb}} = 0\rangle \rightarrow |F_{\text{Rb}} = 2, m_{F,\text{Rb}} = 1\rangle$  transition of the Rb bath.

**Table 1** | Experimental parameters and ratio of mean rates

Parameter	Unidirectional	Bidirectional
$B$ [mG]	460(2)	25(2)
$T$ [nK]	920(24)	492(31)
$n$ [ $10^{13} \text{cm}^{-3}$ ]	0.46(2)	0.51(9)
$R_{+,m_F}/R_{-,m_F}$	$\approx 10^{-5}$	0.21

### Inter-species spin-exchange processes

The Zeeman energy for a bare Cs atom reaches its minimum for  $|m_F = 3\rangle$ , defining the single-atom ground state. However, the situation reverses when the Cs atom is immersed in a bath of Rb atoms in the  $|m_{F,\text{Rb}} = 0\rangle$  state. For this Rb-Cs combination, spin-exchange collisions can exchange one quantum of angular momentum between one atom of the bath and the Cs atom while the total angular momentum is preserved. At the same time, Zeeman energy is exchanged. Due to different atomic Landé factors, the Zeeman splitting of Rb is twice the splitting of Cs. Therefore, the spin- and energy exchange direction is essential and corresponds to two complementary processes in the bath. The process  $|m_F^{\text{Cs}}, m_F^{\text{Rb}}\rangle \rightarrow |m_F^{\text{Cs}} - 1, m_F^{\text{Rb}} + 1\rangle$  is exoergic, and the energy amount corresponding to one Cs atom's Zeeman energy  $\hbar\Delta = \mu_B g_F^{\text{Cs}} B$  is released as kinetic energy and dissipated by subsequent elastic collisions in the bath. The complementary process  $|m_F^{\text{Cs}}, m_F^{\text{Rb}}\rangle \rightarrow |m_F^{\text{Cs}} + 1, m_F^{\text{Rb}} - 1\rangle$  is endoergic, and the kinetic collisional energy of the Cs atom and bath atom must provide the energy amount  $\hbar\Delta$  for this collision to occur. The collisional energy is Maxwell-Boltzmann distributed. For the ultracold temperatures of the bath, the rates for exothermal and endothermal SE collisions,  $R_-$  and  $R_+$ , respectively, have markedly different rates with  $R_- > R_+$ . As a consequence, the definitions of ground and highest excited states invert, and the former bare-atom ground (highest-excited) state, i.e.,  $|m_F = +3\rangle$  ( $|m_F = -3\rangle$ ), defines the impurity's highest excited (ground) state.

### Spin evolution calculation

The evolution of the probability in eigenstate  $|m\rangle$ ,  $p_m$ , is described by the rate equation

$$\dot{p}_m = R_{+,m-1}p_{m-1} + R_{-,m+1}p_{m+1} - (R_{-,m} + R_{+,m})p_m.$$

where  $R_{\pm,m} \equiv R_{m\pm 1,m}$  denotes the transfer rate from eigenstate  $|m\rangle$  to eigenstate  $|m\pm 1\rangle$ . For the unidirectional model discussed in the main text,  $R_{+,m} = 0$ . For the



bidirectional model with state-independent rates,  $R_{\pm,m} \equiv R_{\pm}$ .

For simulating the experimental spin dynamic, the rates are given by  $R_i = \langle n \rangle \sigma_i(B, T) \bar{v}$ , with  $i = m_F \pm 1, m_F$ , mean relative velocity of the colliding atoms  $\bar{v}$ , Cs-Rb density overlap  $\langle n \rangle$  and state-dependent scattering cross section  $\sigma_i$ . The ratio of the mean rates  $R_{+,m_F}/R_{-,m_F}$  in Table 1 shows an experimentally accurately blocking of the endothermal rates  $R_{+,m_F}$  by choice of a large magnetic field.

### **Data availability**

All data supporting the finding of this paper are available from the corresponding author A.W. upon reasonable request.

### **Code availability**

The codes that support the findings of this paper are available from the corresponding author A.E. upon reasonable request.

## Supplemental Material:

### Prethermal memory loss.

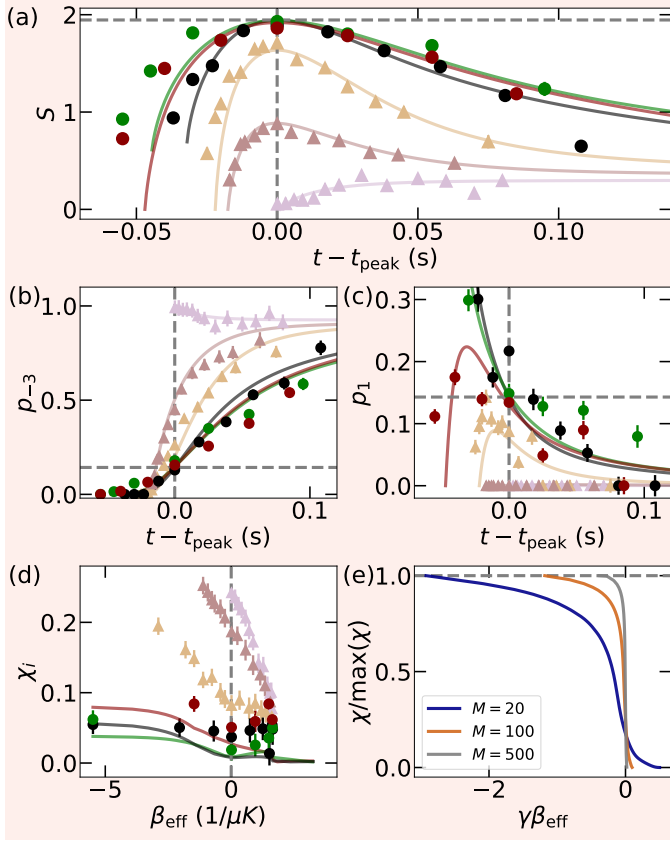


**Figure S1 | Prethermal memory loss in the bidirectional model with state-independent rates.** (a) Experimentally measured (symbols) and simulated (lines) entropy for different initial conditions (color coding as in Fig. 2(b) of the main text) and (b, c) the corresponding spin population of state  $|m_F\rangle$ ,  $p_{m_F}$ , as a function of shifted time (by the peak entropy time  $t_{\text{peak}}$ ) for the bidirectional model. As an illustration, we show two spin components. The dependency of  $\chi$  (see the main text for the definition) on the effective inverse temperature  $\beta_{\text{eff}}$  is shown in (d) for the experiments and in (e) for the theoretical model. Horizontal grey dashed lines mark the maximal entropy  $S_{\text{max}}$  in (a), the population  $1/7$  in (b, c) that corresponds to  $S_{\text{max}}$ , and 1 in (e). Vertical dashed lines mark  $\beta_{\text{eff}} = 0$ .

In the main text, the prethermal memory loss was illustrated for the unidirectional model in Fig. 4. Figure S1 shows the complementary data for the bidirectional model with state-independent rates used in the theoretical model. In Figs. S1(a)-(c), we show the entropy evolution and the population dynamics of two spin states with respect to the shifted time  $t - t_{\text{peak}}$ . We can see that the data with a high peak entropy ( $S_{\text{peak}} \geq 0.98S_{\text{max}}$ , indicated by bullets) show similar behavior for both the entropy evolution and spin dynamics after the system reaches peak entropy ( $t - t_{\text{peak}} > 0$ ). In Fig. S1(d), the difference between

trajectories  $\chi_i$  (see the definition in the main text) is plotted versus effective inverse temperature  $\beta_{\text{eff}}$ . For those trajectories featuring large peak entropies (indicated by bullets),  $\chi_i$  becomes small at the transition  $\beta_{\text{eff}} = 0$  (though the measured signal is not as clear as for the unidirectional model discussed in the main text), whereas it remains large at  $\beta_{\text{eff}} = 0$  for the trajectories with  $S_{\text{peak}} < 0.98S_{\text{max}}$  (indicated by triangles). In Fig. S1(e), we plot normalized  $\chi$  versus  $\beta_{\text{eff}}$  for the theoretical bidirectional model with different system sizes  $M$  at  $\delta S = 0.2$ . One can clearly see that for increasing  $M$ , a sharp transition forms at  $\beta_{\text{eff}} = 0$ .

Prethermal memory loss is also found for both theoretical models, as shown in Fig S2 for systems of size  $M = 50$ . Panels (a) and (b) show the evolution of the entropy with respect to  $t - t_{\text{peak}}$  for various initial conditions (as indicated by the insets). Panels (c-f) show the corresponding evolution for the populations of two different states for each model. One can clearly observe that (only) for those initial conditions for which the peak entropy closely approaches the maximum possible entropy [dashed line in panels (a) and (b)], the results for different initial conditions converge, when approaching  $t = t_{\text{peak}}$ , to remain very similar at all later times.

### Critical exponent.

The critical exponent  $\nu \equiv 1/\alpha$  is extracted by comparing trajectories of different system sizes with  $\gamma\beta_{\text{eff}}M^\alpha \in [-\beta_0, \beta_0]$ . Its value slightly depends on the choice of  $\beta_0$ , as depicted in Fig. S3, which shows the mean difference  $\delta$  between the data of  $M = 20, 100, 500$  with  $\gamma\beta_{\text{eff}}M^\alpha \in [-\beta_0, \beta_0]$  for the unidirectional model. The dashed line marks  $\beta_0 = 2$ , which is shown in the inset of Fig. 3 in the main text.

### Finite-size scaling analysis for the experimental unidirectional model.

To experimentally perform a finite-size scaling analysis, we need to compare results for different system sizes. In the experiments with unidirectional SE, where the spin state  $m_F$  can only be lowered during the evolution, data for system sizes smaller than the full spin manifold can simply be obtained by choosing initial states, where the  $n$  largest  $m_F$  states are not populated. In this way the system size is effectively reduced to  $M - n$ . However, this form of truncation gives rise to rates with a state dependence which becomes highly asymmetric and does not resemble an inverted parabola anymore, as shown in the left middle side panel in Fig. 2. It turns out, the resulting asymmetry prevents the system from reaching close-to-maximum

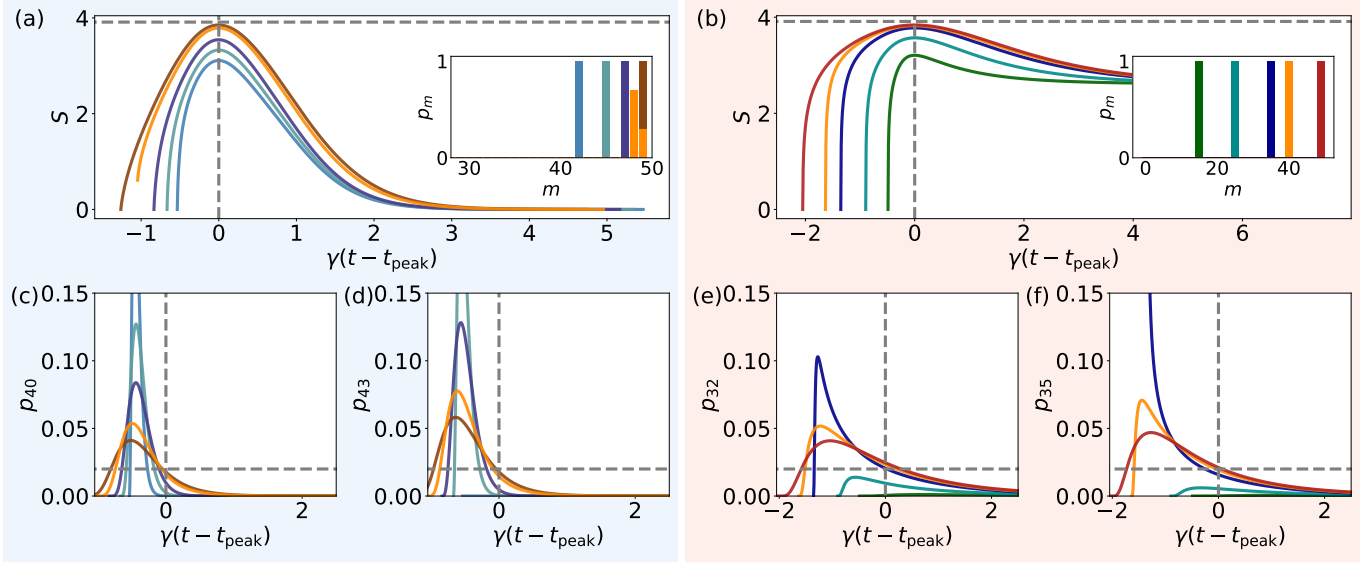


**Figure S2 | Prethermal memory loss in the theoretical models.** (a, b) Entropy  $S$  and (c-f) populations on state  $|m\rangle$ ,  $p_m$ , plotted as a function of shifted time (by the peak entropy time  $t_{\text{peak}}$ ) for different initial conditions as shown in the inset. The horizontal dashed lines in (a, b) mark the maximal entropy  $S_{\text{max}} = \ln M$  with  $M = 50$ , in (c-f) mark  $1/M = 1/50$ . The vertical dashed lines mark the peak entropy time  $t = t_{\text{peak}}$ . Background colors are the same as figures of the main text: blue for the unidirectional model, red for the bidirectional model with state-independent rates.

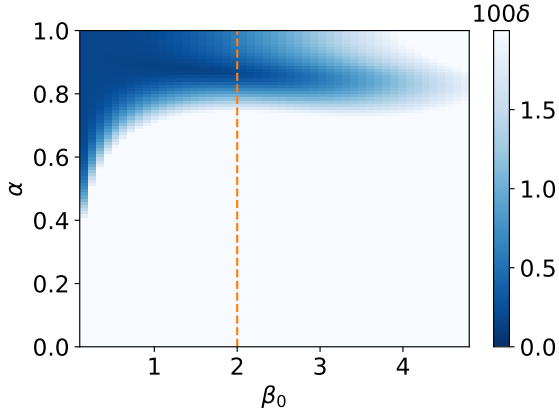


**Figure S3 |** The mean difference  $\delta$  between the data of  $M = 20, 100, 500$  with  $\gamma\beta_{\text{eff}}M^\alpha \in [-\beta_0, \beta_0]$  for the unidirectional model.

peak-entropy values. To keep a rather symmetric shape of the rates and, thus, circumvent this problem, we additionally truncate also the  $n$  lowest  $m_F$  states from the bottom. Thanks to the unidirectional dynamics, this can be achieved effectively by adding the combined population of the discarded  $n$  lowest spin states to that of the lowest effective state,  $m_F = -F + n$ . In this way, we can measure data for systems of effective size  $M_{\text{eff}} = M - 2n$  described by rates with an approximately symmetric state dependence with respect to  $m_F = 0$ .

Figure S4 shows the finite-size scaling analysis for the experimental unidirectional model with  $M_{\text{eff}} = 7, 5, 3$ . The scaling exponent is found to be 0.68, smaller than the value of approximately 0.85 found for the simulations of large systems shown in the main text. However, such a discrepancy is expected in systems of such small size. Namely, the expectation of universal behavior at a phase transition is based on the assumption that, when the length scale  $\xi$  becomes large, the physics will average over the microscopic details of the system, so that they do not matter anymore. In a lattice of a few sites only, this limit can obviously not be achieved yet. A similar discrepancy ( $\nu \approx 0.73$ ) is obtained, when performing the finite-size scaling analysis for the unidirectional theoretical model, using data for  $M = 3, 5, 7$  only.

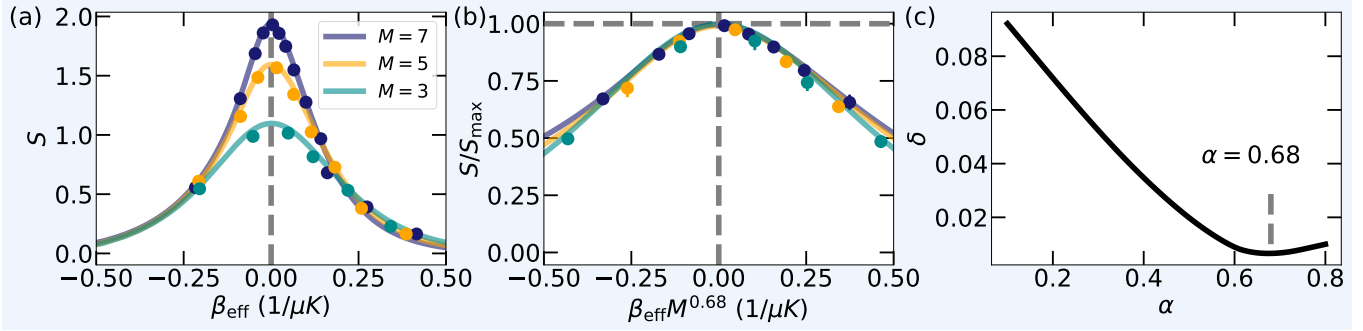


**Figure S4 | Finite-size scaling.** (a) Experimentally measured (symbols) and simulated (lines) entropy plotted as a function of  $\beta_{\text{eff}}$  for different system sizes  $M$ . (b) Normalized entropy vs scaled  $\beta_{\text{eff}}$  using  $\alpha = 0.68$ . (c) The mean difference  $\delta$  between the simulated normalized entropy with  $\beta_{\text{eff}} M^\alpha \in [-0.3, 0.3]$  as a function of the exponent  $\alpha$ , indicating the best-fit exponent  $\alpha = 0.68$ .

### The bidirectional model with state-dependent rate.

In the main text, the bidirectional model was introduced with constant rates  $R_+$  and  $R_-$ . The experiment, however, features  $m_F$ -dependent rates also for the bidirectional model. Therefore, we here consider another bidirectional model, whose transfer rates share the same shape as that in the experiment with the bidirectional spin exchange, as shown in Fig. S5(a). The entropy evolution of this model with  $M = 20$  starting from different initial states (see inset) is shown in Fig. S5(b). One can see the appearance of close-to-maximal entropy when the system starts from high-energy states. Fig. S5(c) shows the entropy evolution for different system sizes. The initial state is set to be the eigenstate which gives rise to the maximal peak entropy among all the eigenstates. For the various system sizes shown, the peak entropy approaches the maximal possible value  $S_{\text{max}}$  in all cases. Analogous to the discussion in the main text, we also show the entropy as a function of the effective inverse temperature  $\beta_{\text{eff}}$  in Fig. S5(d). By scaling  $\beta_{\text{eff}}$  with the system size  $M$  as  $\beta_{\text{eff}}^{0.86}$ , the data for different system sizes collapse in the vicinity of the peak entropy at  $\beta_{\text{eff}} = 0$ , as shown in Fig. S5(e). Note that the exponent 0.86 is roughly the same as that of the two theoretical models discussed in the main text.

### The mapping between the effective inverse temperature $\beta_{\text{eff}}$ and time.

Figure S6 shows the effective inverse temperature  $\beta_{\text{eff}}$  as a function of time (a-c) and shifted time (d-f) for the three theoretical models: the unidirectional model (blue background), the bidirectional model with state-independent rates (red background) and state-dependent rates (yellow background).

### Critical exponent for the effective specific heat

We can define an effective specific heat as  $C \equiv d\langle H \rangle / dT_{\text{eff}}$ , with the effective temperature  $T_{\text{eff}} = 1/\beta_{\text{eff}}$ . In Fig. S7 we show the finite-size scaling analysis for this quantity. Suppose in the thermodynamic limit the specific heat behaves like  $C \propto |\beta_{\text{eff}}|^\alpha$  in the vicinity of the transition at  $\beta_{\text{eff}} = 0$ . Then for a finite system, it should scale like  $C \propto M^{\alpha/\nu} g(\beta_{\text{eff}} M^{1/\nu})$  with the system size, where  $\nu$  is the critical exponent for the length  $\xi$ . The data for different system sizes are expected to collapse in the vicinity of the critical point  $\beta_{\text{eff}} = 0$  by plotting  $C M^{-\alpha/\nu}$  as a function of  $\beta_{\text{eff}} M^{1/\nu}$ . As shown in Figs. S7(d)-(f), the critical exponent  $\alpha$  for the three models is found to be  $\alpha \approx 0.24/0.85 \approx 0.28$ .

### Finite-size scaling for the unidirectional model with time as control parameter.

It is also possible to directly consider the time  $t$ , rather the effective inverse temperature  $\beta_{\text{eff}}$  as the control parameter. In this case, one has to scale the overall strength of the bath-induced rates with the system size  $M$  in such a way that the peak entropy time  $t_{\text{peak}}$  remains finite in the thermodynamic limit, i.e. that it neither approaches infinity nor zero. For the unidirectional model, we achieve this by scaling the rates like  $M^{1.22}$ . Note that such overall scaling of the rates, only changes the time scale of the evolution and not the details of the dynamics. (As a consequence, the dynamics plotted with respect to  $\beta_{\text{eff}}$  remains unchanged, when choosing a different scaling). Under these conditions the divergence of both  $\xi$  and  $S$  occurs at (and within) the finite time  $t_{\text{peak}}$  (see Fig. S8(a)) and, thus, constitutes singular behavior in time corresponding to a dynamical phase transition. In Fig. S8(b) we present a finite-size scaling analysis of this transition and find that the corresponding critical exponent is given by  $1/0.11 \approx 9.1$ .

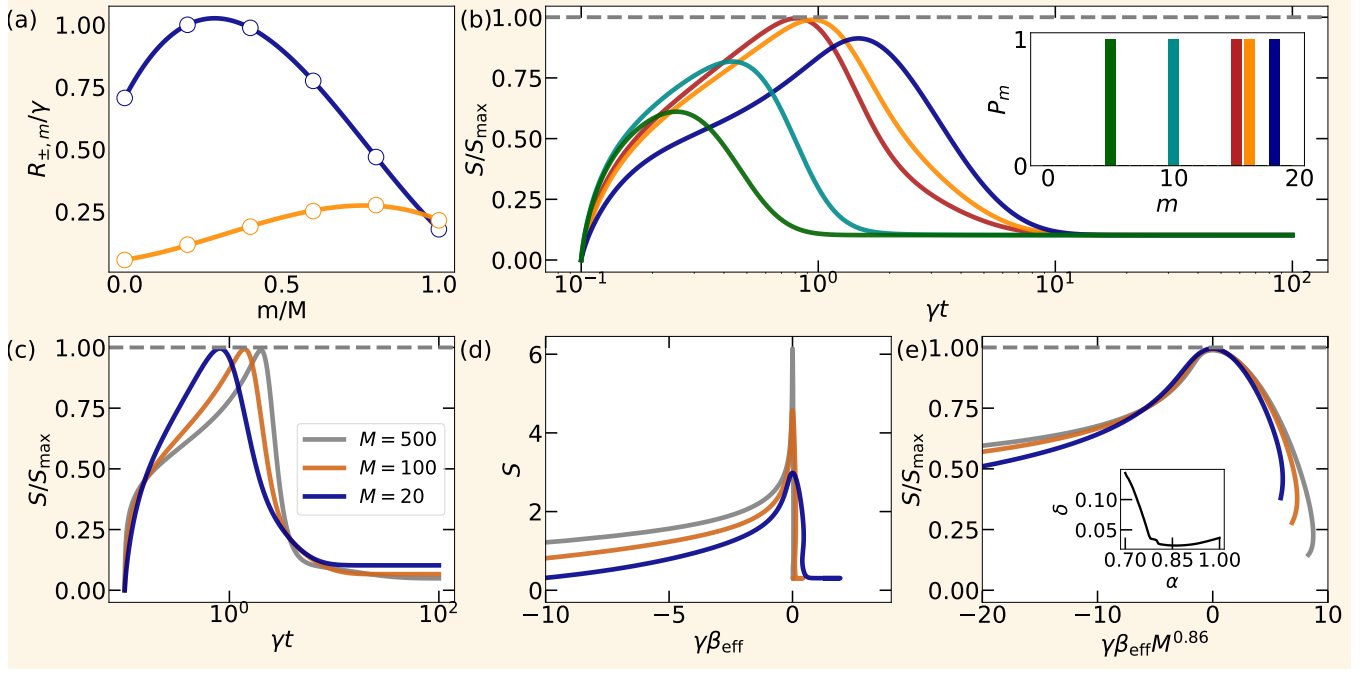


**Figure S5 | Bidirectional model with state-dependent rate.** (a) The normalized transfer rates. The circles denote the spin-exchange rates in the experiments. The solid lines represent the transfer rates in the theoretical model, which is obtained by interpolation of experimental rates. The rates are normalized by the maximal value. (b) Entropy evolution of the model with  $M = 20$  starting from different initial states, as shown in the inset. (c) Entropy evolution for different system sizes. The initial states are the eigenstates whose peak entropy is the maximal among all the eigenstates. (d) Entropy as a function of effective inverse temperature  $\beta_{\text{eff}}$ . (e) Normalized entropy as a function of scaled parameter  $\beta_{\text{eff}} M^\alpha$ , where the exponent  $\alpha$  is fixed by comparing the mean difference  $\delta$  between the data with  $\gamma\beta_{\text{eff}} M^\alpha \in [-2, 2]$ , as shown in the inset.

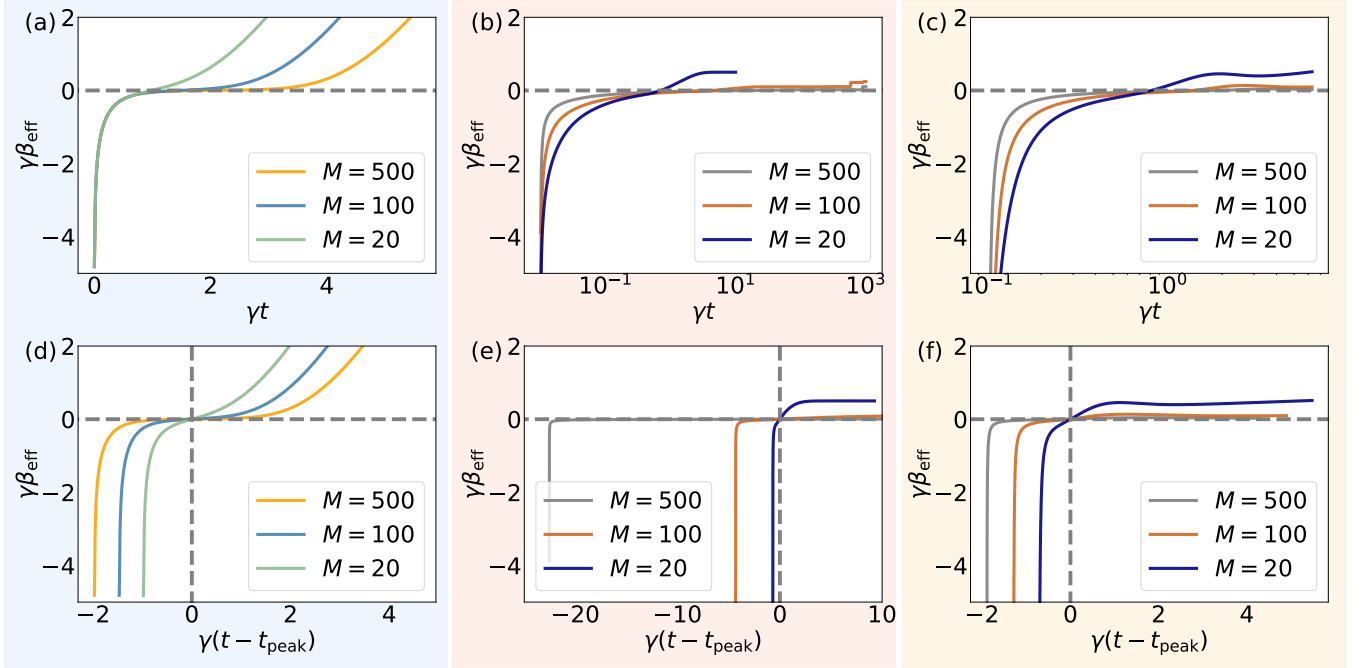


**Figure S6 |** The effective inverse temperature  $\beta_{\text{eff}}$  as a function of time (a-c) or shifted time (d-f) for the unidirectional model (blue background), the bidirectional model with state-independent rates (red background) and with state-dependent rates (yellow background).

### Experimental parameters.

Tables S1 and S2 provide the experimental parameters for each data set of the unidirectional and bidirectional model

realized at magnetic fields of 460 mG and 25 mG, respectively. The initial population of each data set is illustrated

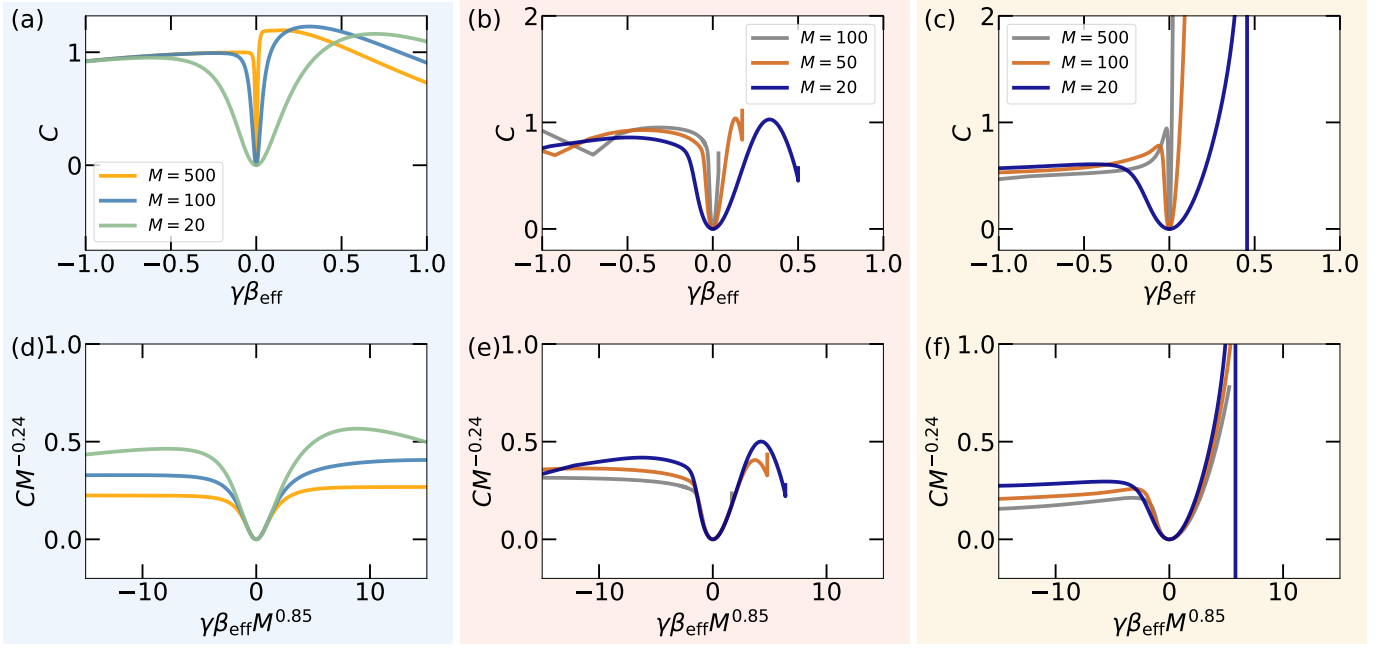


**Figure S7 | Finite-size scaling for the effective specific heat  $C \equiv d\langle H \rangle / dT_{\text{eff}}$ .** (a)-(c) show  $C$  as a function of  $\beta_{\text{eff}}$  for the unidirectional model (blue background), the bidirectional model with state-independent rates (red background) and with state-dependent rates (yellow background), respectively. The nonsingularity appearing after the peak entropy (for  $\beta_{\text{eff}} > 0$ ) is attributed to numerical error due to the slow change of the effective temperature  $T_{\text{eff}}$  when the system approaches the steady state. (d)-(f) show the corresponding results for scaled  $C$  as a function of scaled  $\beta_{\text{eff}}$ . Suppose in the thermodynamic limit the specific heat behaves like  $C \propto |\beta_{\text{eff}}|^\alpha$  in the vicinity of the transition at  $\beta_{\text{eff}} = 0$ . Then for a finite system, it should scale like  $C \propto M^{\alpha/\nu} g(\beta_{\text{eff}} M^{1/\nu})$  with the system size, where  $\nu$  is the critical exponent for the length  $\xi$ . The data for different system sizes are expected to collapse in the vicinity of the critical point  $\beta_{\text{eff}} = 0$  by plotting  $CM^{-\alpha/\nu}$  as a function of  $\beta_{\text{eff}} M^{1/\nu}$ . As shown in the (d)-(f), the critical exponent  $\alpha$  is found to be  $\alpha \approx 0.24/0.85 \approx 0.28$ .

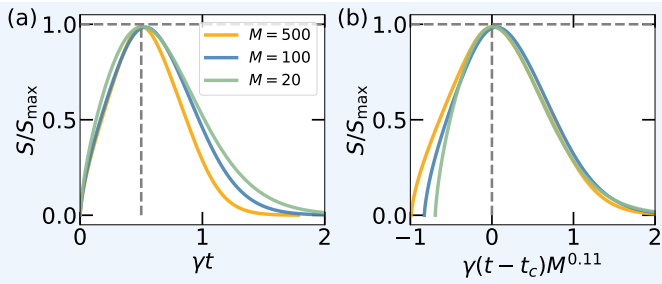


**Figure S8 | Finite-size scaling for the unidirectional model with time as control parameter.** (a) The normalized entropy as a function of time for different system sizes. The overall strength of the bath-induced rates scales with the system size as  $M^{1.22}$ . The vertical dashed line marks  $\gamma t_c = 0.5$ . (b) The normalized entropy as a function of the scaled shifted time (by  $t_c$ ).

and color-coded as histogram in Fig. 2 of the main text. For simplicity the tables contain the two most populated initial states. The last missing percents of the initial population distribute over the unspecified states in the tables. Table 1 of Methods gives the mean values of the listed temperatures and densities.

**Table S1 | Experimental parameters of the individual measurements for the unidirectional system, i.e.  $B = 460(2)$  mG.**

$p_{m_F}(t=0)$	$T$ [nK]	$n$ [ $10^{13}\text{cm}^{-3}$ ]
$p_0 = 1.00(4)$	900(75)	0.44(9)
$p_3 = 0.98(3)$		
	950(67)	0.44(8)
$p_2 = 0.02(1)$		
$p_2 = 0.90(2)$		
	950(52)	0.49(8)
$p_1 = 0.06(1)$		
$p_1 = 0.95(2)$		
	900(57)	0.45(6)
$p_0 = 0.05(1)$		
$p_2 = 0.51(3)$		
	900(52)	0.47(7)
$p_3 = 0.48(2)$		



**Table S2** | Experimental parameters of the individual measurements for the bidirectional system, i.e.  $B = 25(2)$  mG.

$p_{m_F}(0)$	$T$ [nK]	$n$ [ $10^{13}\text{cm}^{-3}$ ]
$p_1 = 0.66(3)$	500(87)	0.41(16)
$p_2 = 0.25(2)$		
$p_2 = 0.78(3)$	450(43)	0.55(12)
$p_1 = 0.11(1)$		
$p_2 = 0.49(3)$	525(55)	0.63(12)
$p_1 = 0.44(2)$		
$p_0 = 0.85(3)$	500(47)	0.53(12)
$p_{-1} = 0.07(1)$		
$p_{-2} = 0.93(4)$	525(55)	0.38(11)
$p_{-3} = 0.06(1)$		
$p_{-3} = 0.99(4)$	450(54)	0.58(15)
$p_{-2} = 0.01(1)$		